





Cite this: *J. Mater. Chem. A*, 2025, **13**, 13195

## Transition metal–phenanthroline intercalated montmorillonite as efficient electrocatalysts for the oxygen evolution reaction†

In Seon Lee,  ‡ Jae Ryeol Jeong,  ‡ Cu Dang Van  and Min Hyung Lee  \*

With the escalating climate crisis, the development of efficient, low-cost energy sources with minimal carbon footprints is more critical than ever. Among various green energy solutions, hydrogen production via water electrolysis has garnered significant attention due to the abundance of water and the cleanliness of hydrogen as a product. However, the widespread adoption of this technology is hindered by the sluggish kinetics of the oxygen evolution reaction (OER) at the anode, which compromises its economic viability compared to conventional hydrogen production methods. Addressing this challenge requires the development of highly efficient OER electrocatalysts to reduce overpotential and improve reaction kinetics. In this study, we present a novel strategy for synthesizing OER electrocatalysts by intercalating organo-metallic complexes of 1,10-phenanthroline (Phen) coordinated with Ni, Co, and Fe into the interlayers of montmorillonite (MMT) clay. Structural analyses using X-ray diffraction (XRD), small-angle X-ray scattering (SAXS), and transmission electron microscopy (TEM) confirmed the successful insertion of the complexes, evidenced by an increase in the interlayer spacing of the MMT. Electrochemical performance evaluations revealed that MMT:Co(Phen)<sub>2</sub> exhibited the best OER activity, achieving an overpotential of 313 mV at a current density of 10 mA cm<sup>−2</sup>, along with excellent stability over 50 hours of operation.

Received 10th January 2025  
Accepted 23rd March 2025

DOI: 10.1039/d5ta00244c

rsc.li/materials-a

## 1. Introduction

The rapid increase of energy demands driven by industrialization and population growth necessitates the development of sustainable and clean energy alternatives to reduce reliance on fossil fuels and mitigate carbon emissions.<sup>1,2</sup> While solar and wind energy are promising renewable sources, their inherent intermittency and geographic limitations create challenges in maintaining a stable and continuous energy supply, necessitating efficient energy storage and conversion technologies.<sup>3–5</sup> As a solution, electrochemical energy conversion has gained attention for its ability to convert and store energy in the form of chemical fuels.<sup>6,7</sup>

Among electrochemical energy conversion technologies, water splitting has emerged as a clean and sustainable method for hydrogen production.<sup>8</sup> With advancements in efficiency and stability, this approach has the potential to replace conventional steam reforming, the dominant industrial hydrogen production method, which generates significant CO<sub>2</sub> emissions.<sup>9,10</sup> However, its efficiency is hindered by the OER, which

involves sluggish four-electron transfer kinetics at the anode, requiring high overpotentials to drive the reaction. In contrast, the hydrogen evolution reaction (HER) at the cathode proceeds with relatively lower activation energy.<sup>11–13</sup> Due to these kinetic limitations, electrocatalysts are essential for enhancing OER efficiency and reducing energy losses.

Noble metal catalysts such as IrO<sub>2</sub> and RuO<sub>2</sub> are widely regarded as the benchmark for OER due to their excellent catalytic activity. However, their high cost, scarcity, and stability concerns under operational conditions limit their large-scale applicability. For instance, RuO<sub>2</sub> undergoes oxidative degradation at high potentials, while IrO<sub>2</sub> faces dissolution challenges during prolonged OER operation. Consequently, the development of cost-effective, stable, and efficient OER electrocatalysts is imperative to advance sustainable hydrogen production.<sup>14–16</sup>

Recent studies have demonstrated the potential of organo-metallic complexes such as [Co(bpy)<sub>3</sub>]<sup>3+/2+</sup> and [Co(phen)<sub>3</sub>]<sup>3+/2+</sup> as electron mediators for overall water splitting under visible light.<sup>17</sup> These complexes exhibit promising catalytic activity; however, their direct application in electrocatalysis is significantly hindered by oxidative and chemical degradation, resulting in limited durability.<sup>18</sup> Therefore, a robust support material that can stabilize these complexes while preserving their catalytic properties is essential.

MMT, a naturally abundant layered clay mineral, presents an ideal platform for enhancing the stability and performance of

Department of Applied Chemistry, Kyung Hee University, Yongin, Gyeonggi 17104, Korea. E-mail: minhlee@khu.ac.kr

† Electronic supplementary information (ESI) available. See DOI: <https://doi.org/10.1039/d5ta00244c>

‡ These authors contributed equally to this work.



organo-metallic complexes in OER electrocatalysis. Its 2 : 1 layered structure composed of an octahedral alumina sheet sandwiched between two tetrahedral silica sheets<sup>19–23</sup> provides high cation exchange capacity, large interlayer spacing, and porous framework, making it well-suited for intercalating and protecting active catalyst species.<sup>24,25</sup> By encapsulating organo-metallic complexes within the MMT framework, it is possible to mitigate oxidative degradation, enhance charge transfer, and improve overall catalytic efficiency.<sup>26</sup> While MMT has been extensively studied in wastewater treatment<sup>27,28</sup> and antimicrobial applications, its potential in electrocatalysis remains largely unexplored.<sup>29,30</sup>

In this study, we leverage the cation exchange capacity of MMT to intercalate organo-metallic complexes of Phen with Ni, Co, and Fe, forming novel OER electrocatalysts. Structural analysis *via* XRD and TEM confirms the successful integration of the complexes, leading to enhanced basal spacing, increased surface area, and improved porosity while preserving the layered framework of MMT.<sup>31–33</sup> Among the synthesized catalysts, MMT:Co(Phen)<sub>2</sub> demonstrates the best performance, achieving an overpotential of 313 mV at 10 mA cm<sup>−2</sup> with excellent stability over 50 hours. This work underscores the potential of organo-metallic complexes intercalated into MMT as next-generation OER electrocatalysts, providing a scalable, cost-effective, and environmentally sustainable solution for green hydrogen production.

## 2. Results and discussion

MMT:M(Phen)<sub>2</sub> complexes (M = Ni, Co, and Fe) incorporating M(Phen)<sub>2</sub> in MMT were synthesized by first modifying Na-MMT with Phen *via* cation exchange in ethanol followed by reaction with metal nitrate precursors (see Materials and methods and Fig. 1). The formation of M(Phen)<sub>2</sub> complexes and their incorporation into the MMT were confirmed by Fourier-transform infrared spectroscopy (FT-IR) (Fig. 2a and Table S1†). In the spectra of Na-MMT and MMT:M(Phen)<sub>2</sub>, the stretching and bending vibrations of Si–O–Si and Si–O within the silicon-oxygen tetrahedra of MMT were observed at approximately 1046 cm<sup>−1</sup> and 468 cm<sup>−1</sup>, respectively. The peak around 526 cm<sup>−1</sup> is attributed to the bending vibration of Si–O–Al in the tetrahedral layer. The stretching and bending vibrations observed in the FT-IR spectra of MMT:M(Phen)<sub>2</sub> align with the

characteristic bands of MMT, suggesting that the intercalation of MMT:M(Phen)<sub>2</sub> complexes into the interlayers preserved the structural integrity of the MMT framework. Additionally, the shift in OH stretching vibration from 3455 cm<sup>−1</sup> in Na-MMT to 3440 cm<sup>−1</sup> in MMT:M(Phen)<sub>2</sub> suggests stronger hydrogen bonding interactions between transition metals and the MMT. This finding aligns with the observed shift in the C–N stretching band from 1345 cm<sup>−1</sup> in free Phen to 1384 cm<sup>−1</sup> in MMT:M(Phen)<sub>2</sub>, confirming the coordination of transition metals with nitrogen atoms from Phen.<sup>34</sup>

XRD further confirmed the successful intercalation of M(Phen)<sub>2</sub> complexes within the MMT layers (Fig. 2b). A distinct shift in the (001) plane was observed, indicating expansion of the interlayer spacing from 12.8 Å (Na-MMT)<sup>35</sup> to 18.5 Å (MMT:Phen) due to the incorporation of Phen molecules. After coordination with transition metals, the basal spacing (*d*<sub>001</sub>) slightly reduced to 17.2 Å in MMT:Ni(Phen)<sub>2</sub>, 17.0 Å in MMT:Co(Phen)<sub>2</sub>, and 16.8 Å in MMT:Fe(Phen)<sub>2</sub>, suggesting further structural reorganization upon M(Phen)<sub>2</sub> complex formation. Despite these changes, the layered integrity of MMT was maintained.<sup>36</sup>

To quantify the interlayer changes, the interlayer spacing height was estimated by subtracting the thickness of the aluminosilicate layer (9.6 Å) from the basal spacing, as shown in Table S2.† Na-MMT exhibited an interlayer spacing height of approximately 3.2 Å, reflecting the presence of hydrated Na<sup>+</sup> ions (hydrated radius ~2.76 Å).<sup>37</sup> Upon intercalation with Phen, the spacing height increased significantly to 8.9 Å, consistent with the molecular height of Phen (~9.4 Å), suggesting a monolayer arrangement of Phen within the MMT interlayers.<sup>37,38</sup> After coordination with transition metals, the interlayer spacing heights for MMT:Ni(Phen)<sub>2</sub>, MMT:Co(Phen)<sub>2</sub>, and MMT:Fe(Phen)<sub>2</sub> were measured as 7.6 Å, 7.4 Å, and 7.2 Å, respectively. This slight reduction compared to MMT:Phen suggests structural distortions upon metal coordination, likely due to the formation of M(Phen)<sub>2</sub> complexes within the inter-layer region.

To further elucidate the structural impact of intercalating organo-metallic complexes into the MMT framework, SAXS analysis was performed (Fig. S1 and Table S3†). SAXS results showed a noticeable shift in scattering peaks for the MMT:M(Phen)<sub>2</sub> samples compared to Na-MMT, indicating an expansion of the interlayer spacing due to the incorporation of

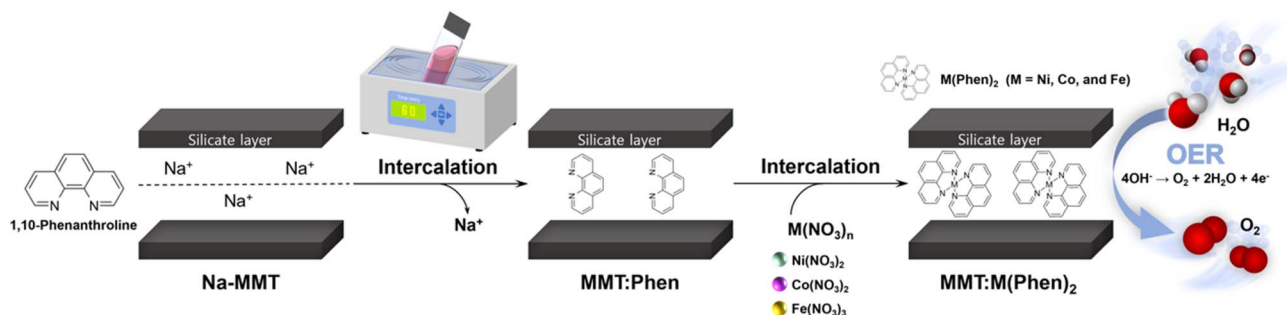


Fig. 1 Schematic illustration of the synthesis and electrocatalytic application of MMT:M(Phen)<sub>2</sub> for the OER.



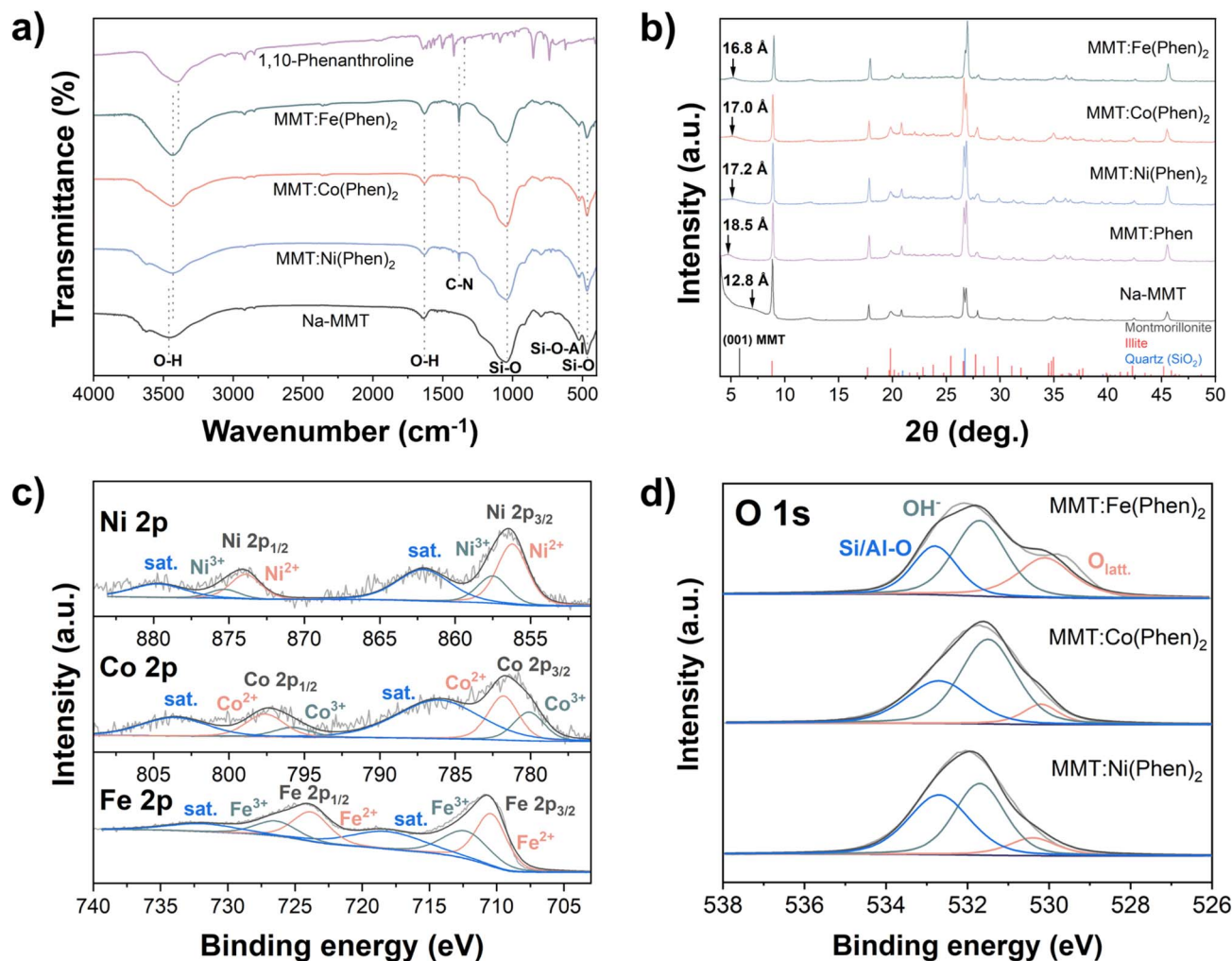


Fig. 2 (a) FT-IR spectra and (b) XRD patterns for Na-MMT, MMT:Phen, and MMT:M(Phen)<sub>2</sub> composites. High-resolution XPS spectra of (c) Ni 2p, Co 2p, Fe 2p, and (d) O 1s of MMT:M(Phen)<sub>2</sub>.

M(Phen)<sub>2</sub> complexes. Specifically, the primary scattering peak of Na-MMT appeared at  $q = 0.488 \text{ \AA}^{-1}$  ( $d$ -spacing =  $12.9 \text{ \AA}$ ), while intercalated systems exhibited shifted peaks, corresponding to  $d$ -spacings of  $17.0$ – $17.4 \text{ \AA}$ . These results confirm that the successful intercalation of M(Phen)<sub>2</sub> complexes within the MMT, further supporting the XRD and HR-TEM analyses. The expanded interlayer spacing is beneficial for mass transport and charge transfer, key factors in electrocatalytic applications.<sup>39</sup> The uniform dispersion of M(Phen)<sub>2</sub> complexes within the MMT framework enhances the accessibility of active sites, contributing to improved electrochemical performance.

X-ray photoelectron spectroscopy (XPS) analysis was conducted to investigate the surface chemical states and elemental composition of the MMT:M(Phen)<sub>2</sub> composites (Fig. 2c, d and S2†). The transition metals (Ni, Co, and Fe), C and N from Phen, and the characteristic Si, Al, Mg, and O peaks from MMT confirmed the incorporation of M(Phen)<sub>2</sub> complexes within the MMT framework (Fig. S2a–c†). The high-resolution C 1s spectra provided further insight into the bonding

characteristics of the M(Phen)<sub>2</sub> complexes within MMT (Fig. S2d†). The deconvoluted peaks at approximately  $284.8$ ,  $286.1$ ,  $287.6$ , and  $289.1 \text{ eV}$  correspond to C–C/C–H, C–O, C=O/C=N, and O–C=O functional groups, respectively.<sup>40,41</sup> The presence of C=N signals indicates the incorporation of M(Phen)<sub>2</sub> within the MMT framework. While the peak positions remain largely consistent across the different metal complexes, minor shifts in binding energy are attributed to variations in the metal coordination environment and interactions with the MMT matrix.

The high-resolution XPS spectra of the 2p regions for the transition metals revealed coexistence of mixed oxidation states ( $M^{2+}/M^{3+}$ ) for all analyzed transition metals in the M(Phen)<sub>2</sub> complexes embedded in MMT (Fig. 2c). The spin-orbit splitting between the  $2p_{3/2}$  and  $2p_{1/2}$  peaks, along with the presence of satellite peaks, further supports strong interactions between the transition metals and the surrounding environment, which can influence charge transfer properties in electrocatalytic applications.<sup>42,43</sup>





Fig. 2d exhibits the high-resolution XPS spectrum deconvolution of the O 1s region for the MMT:M(Phen)<sub>2</sub> composites. Three primary peaks at 530.4, 531.7, and 532.7 eV correspond to lattice oxygen (O<sub>latt.</sub>) in M–O bonds, surface hydroxyl groups (OH<sup>−</sup>), and Si/Al–O bonds from MMT, respectively.<sup>44–46</sup> The relatively higher intensity of the OH<sup>−</sup> peak compared to the Si/Al–O peak indicates significant contributions from hydroxyl groups in the MMT structure. The presence of hydroxyl species suggests potential involvement in catalytic reactions, as surface OH<sup>−</sup> groups can facilitate charge transport and enhance electrocatalytic performance. The peak intensities of O<sub>latt.</sub> remained relatively stable across different composites, indicating that the MMT framework remained structurally intact during the intercalation process.

The surface morphology of MMT composites was examined using scanning electron microscopy (SEM) images to examine structural changes upon intercalation of M(Phen)<sub>2</sub> complexes (Fig. 3a–e). SEM images reveal that Na-MMT exhibits a thin-layered structure with large flakes, characteristic of its crystalline framework. After modification with M(Phen)<sub>2</sub>, the morphology undergoes a noticeable transformation with increased surface roughness and porosity observed in MMT:M(Phen)<sub>2</sub> composites. The formation of smaller, more dispersed flakes suggests that ultrasonic treatment effectively prevents aggregation, while the intercalation of M(Phen)<sub>2</sub> complexes alters surface characteristics, potentially improving electrolyte accessibility and charge transfer efficiency.<sup>47,48</sup> To further investigate the distribution of elements within the composites, energy dispersive X-ray spectroscopy (EDS) mapping was performed (Fig. S3†). The uniform distribution of Si and O confirms that the MMT framework remains intact post-modification. Additionally, the limited and discrete presence of Ni, Co, Fe, and N verifies the successful intercalation of M(Phen)<sub>2</sub> complexes. These results highlight the structural integrity of MMT is preserved while enabling efficient metal complex incorporation, which is essential for maintaining

homogeneous active site distribution in electrocatalytic applications.

To examine the structural impact of M(Phen)<sub>2</sub> intercalation at the nanoscale, high-resolution transmission electron microscopy (HR-TEM) was performed (Fig. 3f–j). The HR-TEM images of MMT composites reveal distinct basal plane fringes, confirming the retention of the layered structure of MMT. The measured interlayer distances were 13.1 Å for Na-MMT, 18.5 Å for MMT:Phen, and 16.6–17.1 Å for MMT:M(Phen)<sub>2</sub>, respectively. The slight reduction in *d*-spacing after metal coordination indicates that M(Phen)<sub>2</sub> complexes adjust their orientation within the interlayer space, likely due to metal–Phen interactions stabilizing the structure. These findings correlate well with XRD data (Fig. 2b) where shifts in the (001) diffraction peaks further confirm successful intercalation. Elemental mapping using TEM-EDS analyses at nanoscale in Fig. S4† also confirms co-localization of transition metals and nitrogen within the MMT, indicating uniform dispersion of catalytic species. The absence of excess metal clusters suggests that the intercalation process successfully prevents phase segregation, ensuring a homogeneous distribution of active sites. This controlled dispersion is expected to enhance charge transport and catalytic efficiency, which are key factors for improving OER performance.

The nitrogen adsorption/desorption measurements at 77 K were performed to evaluate the porosity of the MMT:M(Phen)<sub>2</sub> nanocomposites (Fig. S5†). The adsorption isotherms exhibit type IV profiles with H3 hysteresis loops, characteristic of mesoporous materials with slit-like pores, which aligns with the layered structure of MMT (Fig. S5a–c†).<sup>49,50</sup> The similarity of these isotherms to those of unmodified MMT K10 suggests that the mesoporous framework remains intact following intercalation, as further supported by XRD analysis.<sup>51</sup> The Barrett–Joyner–Halenda (BJH) pore size distribution curves support the mesoporous characteristics of the composites (Fig. S5d†). The specific surface areas, mesopore volumes, and total pore

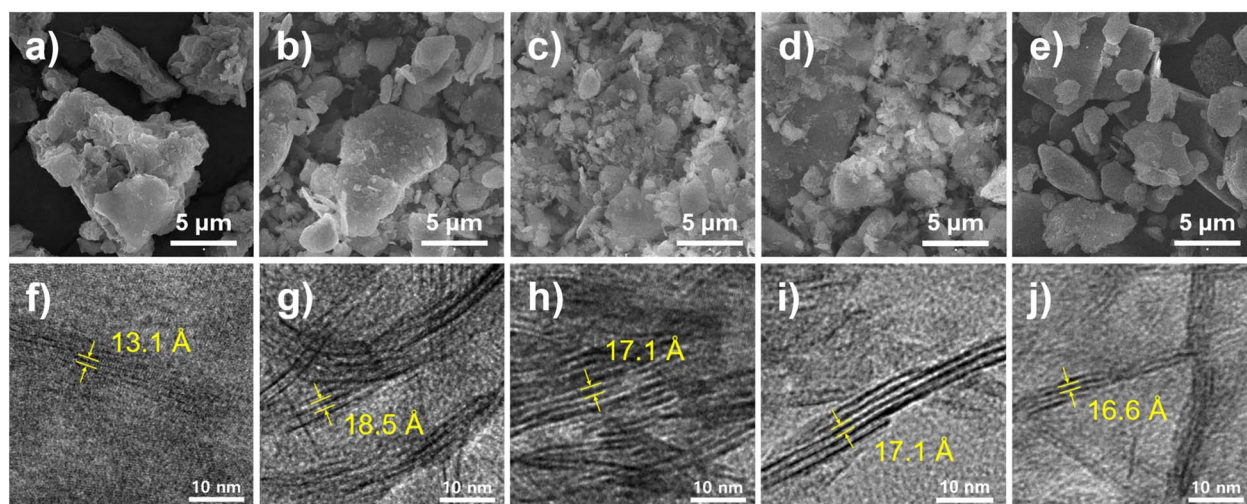


Fig. 3 SEM images and TEM images of (a and f) Na-MMT, (b and g) MMT:Phen, (c and h) MMT:Ni(Phen)<sub>2</sub>, (d and i) MMT:Co(Phen)<sub>2</sub>, and (e and j) MMT:Fe(Phen)<sub>2</sub>.



volumes of the samples are summarized in Table S4.† Despite maintaining mesoporosity, BET analysis reveals a notable reduction of specific surface area ( $S_{\text{BET}}$ ) and total pore volume ( $V_{\text{tot}}$ ) in MMT:M(Phen)<sub>2</sub> composites ( $S_{\text{BET}}$  of 124.71–137.61 m<sup>2</sup> g<sup>−1</sup> and a  $V_{\text{tot}}$  of 0.2932–0.3509 cm<sup>3</sup> g<sup>−1</sup>) compared with unmodified MMT ( $S_{\text{BET}}$  of 242.21 m<sup>2</sup> g<sup>−1</sup> and a  $V_{\text{tot}}$  of 0.41 cm<sup>3</sup> g<sup>−1</sup>).<sup>51</sup> These reductions in the MMT:M(Phen)<sub>2</sub> composites are attributed to partial pore blocking by the intercalation of M(Phen)<sub>2</sub> complexes and larger exchanged cations.<sup>52</sup> However, the composites still retain sufficient porosity, which is beneficial for electrolyte accessibility and ion transport, crucial for catalytic applications.

The thermogravimetric analysis (TGA) profiles of Na-MMT and MMT:Phen composites are presented to study thermal stability, organic content, and structural water within the materials (Fig. S6†). The TGA curve of Na-MMT exhibits two distinct stages of weight loss. The initial weight loss of approximately 7.8% at 106.1 °C corresponds to the removal of adsorbed and structural water from the interlayer spaces of the MMT. At higher temperatures, a secondary weight loss of about 3.8% occurs at 676.0 °C, which is attributed to the dihydroxylation of the clay structure, a characteristic thermal event in MMT. In comparison, the MMT:Phen composite exhibits three stages of thermal degradation, reflecting the incorporation of organic molecules into MMT. The first weight loss of approximately 4.5% at 102.9 °C is associated with the removal of water, similar to Na-MMT but with a reduced magnitude, likely due to partial replacement of interlayer water by Phen. The second, distinct weight loss of around 10.0% at 426.1 °C corresponds to the thermal degradation of the Phen, confirming its successful intercalation within the MMT layers. Finally, a minor weight loss of about 3.1% at 715.1 °C is observed, attributed to the dihydroxylation of the MMT structure, consistent with the thermal decomposition behavior of MMT.

The OER catalytic performance of the prepared MMT:M(Phen)<sub>2</sub> composites was evaluated using various electrochemical measurements in 1 M KOH with a three-electrode system (Fig. 4). The linear sweep voltammetry (LSV) curves show that the type of transition metal significantly influences OER activity (Fig. 4a). Among the MMT:M(Phen)<sub>2</sub> composites, MMT:Co(Phen)<sub>2</sub> exhibits the lowest overpotential at 10 mA cm<sup>−2</sup> ( $\eta_{10}$  = 313 mV), outperforming MMT:Ni(Phen)<sub>2</sub> ( $\eta_{10}$  = 320 mV) and MMT:Fe(Phen)<sub>2</sub> ( $\eta_{10}$  = 361 mV) (Fig. 4b). The superior performance of MMT:Co(Phen)<sub>2</sub> highlights the synergistic interaction between the Co center and the Phen ligand, which enhances catalytic efficiency. In contrast, MMT:Fe(Phen)<sub>2</sub> exhibits a higher overpotential, indicating limited synergy with the ligand and less efficient charge transfer. Notably, both MMT:Ni(Phen)<sub>2</sub> and MMT:Co(Phen)<sub>2</sub> catalysts exhibit lower overpotentials than those of the unmodified MMT or MMT:Phen (Fig. S7a†), underscoring the advantages of transition metal incorporation in enhancing OER activity. Further analysis of the OER kinetics, as shown in Fig. 4c, reveals that MMT:Ni(Phen)<sub>2</sub> and MMT:Co(Phen)<sub>2</sub> exhibit low Tafel slopes of 47 mV dec<sup>−1</sup> and 43 mV dec<sup>−1</sup>, respectively. These values indicate rapid charge transfer and favorable reaction kinetics

compared to MMT:Fe(Phen)<sub>2</sub>, which exhibits a higher Tafel slope of 54 mV dec<sup>−1</sup>, reflecting slower kinetics (Fig. 4c).

To assess the charge transfer efficiency, electrochemical impedance spectroscopy (EIS) measurements were performed for MMT:M(Phen)<sub>2</sub> (Fig. 4d). The charge-transfer resistance ( $R_{\text{ct}}$ ) values reveal that MMT:Ni(Phen)<sub>2</sub> ( $R_{\text{ct}}$  = 13.5  $\Omega$  cm<sup>2</sup>) and MMT:Co(Phen)<sub>2</sub> ( $R_{\text{ct}}$  = 22.1  $\Omega$  cm<sup>2</sup>) exhibit significantly lower  $R_{\text{ct}}$  values compared to MMT:Fe(Phen)<sub>2</sub> ( $R_{\text{ct}}$  = 1450.4  $\Omega$  cm<sup>2</sup>), confirming enhanced charge transfer capabilities in Ni- and Co-based catalysts. In comparison, bare carbon paper ( $R_{\text{ct}}$  = 274.1  $\Omega$  cm<sup>2</sup>), Na-MMT ( $R_{\text{ct}}$  = 1858.6  $\Omega$  cm<sup>2</sup>), and MMT:Phen ( $R_{\text{ct}}$  = 167.3  $\Omega$  cm<sup>2</sup>) exhibit significantly higher  $R_{\text{ct}}$  values, indicating that transition metal incorporation plays a critical role in improving conductivity and catalytic activity (Fig. S7b and Table S5†).

The electrochemical surface area (ECSA) of MMT:M(Phen)<sub>2</sub> composites was evaluated by the electrochemical double-layer capacitance ( $C_{\text{dl}}$ ) determined from the cyclic voltammetry (CV) measurements in the non-Faradaic region (0.92 to 1.02 V vs. RHE) at different scan rates (Fig. S8a–c†). The calculated  $C_{\text{dl}}$  values were determined to be 0.039, 0.055, and 0.057 mF cm<sup>−2</sup> for MMT:Ni(Phen)<sub>2</sub>, MMT:Co(Phen)<sub>2</sub>, and MMT:Fe(Phen)<sub>2</sub>, respectively (Fig. S8d†). By normalizing the current density with respect to the ECSA (Fig. 4e), variations arising from differences in electrode morphology and exposed surface area were minimized, allowing for a more precise comparison of intrinsic catalytic activity. Despite MMT:Fe(Phen)<sub>2</sub> exhibiting the highest  $C_{\text{dl}}$  value among the samples, its inferior OER performance was evident from its lowest ECSA-normalized current density ( $j_{\text{ECSA}}$  = 3.16 mA cm<sup>−2</sup> at overpotential of 350 mV) and highest Tafel slope. In contrast, MMT:Co(Phen)<sub>2</sub>, with a slightly lower  $C_{\text{dl}}$ , demonstrated superior OER activity due to enhanced intrinsic catalytic properties and electronic interactions between the transition metal and Phen ligand achieving a  $j_{\text{ECSA}}$  value of 37.04 mA cm<sup>−2</sup>. The lower  $j_{\text{ECSA}}$  value of MMT:Ni(Phen)<sub>2</sub> (32.63 mA cm<sup>−2</sup>) suggests relatively lower availability of active sites.

To further evaluate the intrinsic activity of the catalysts, the turnover frequency (TOF) values were determined by assuming that the concentration of metal ions as estimated from inductively coupled plasma mass spectrometry (ICP-MS) results (Table S6†) corresponds to the amount of transition metal. A comparison of TOF values at an overpotential of 350 mV revealed that MMT:Co(Phen)<sub>2</sub> exhibited the highest TOF (0.966 s<sup>−1</sup>), outperforming MMT:Ni(Phen)<sub>2</sub> (0.487 s<sup>−1</sup>) and MMT:Fe(Phen)<sub>2</sub> (0.00577 s<sup>−1</sup>) (Fig. 4f). These results indicate that MMT:Co(Phen)<sub>2</sub> exhibited the highest OER intrinsic activity, which is consistent with the above ECSA-normalized current density trends.

The superior OER performance of MMT:Co(Phen)<sub>2</sub> compared to MMT:Ni(Phen)<sub>2</sub> and MMT:Fe(Phen)<sub>2</sub> can be explained by its electronic structure and metal–ligand coordination effects. Fe(Phen)<sub>2</sub> (d<sup>6</sup>, low-spin) strongly interacts with oxygen intermediates due to its empty  $e_g$  orbital.<sup>53</sup> Since there are no electrons in the  $e_g$  orbital, oxygen species can strongly donate electrons to the metal center without significant repulsion, leading to enhanced orbital overlap. Since this strong interaction excessively stabilizes the \*O species, the catalytic



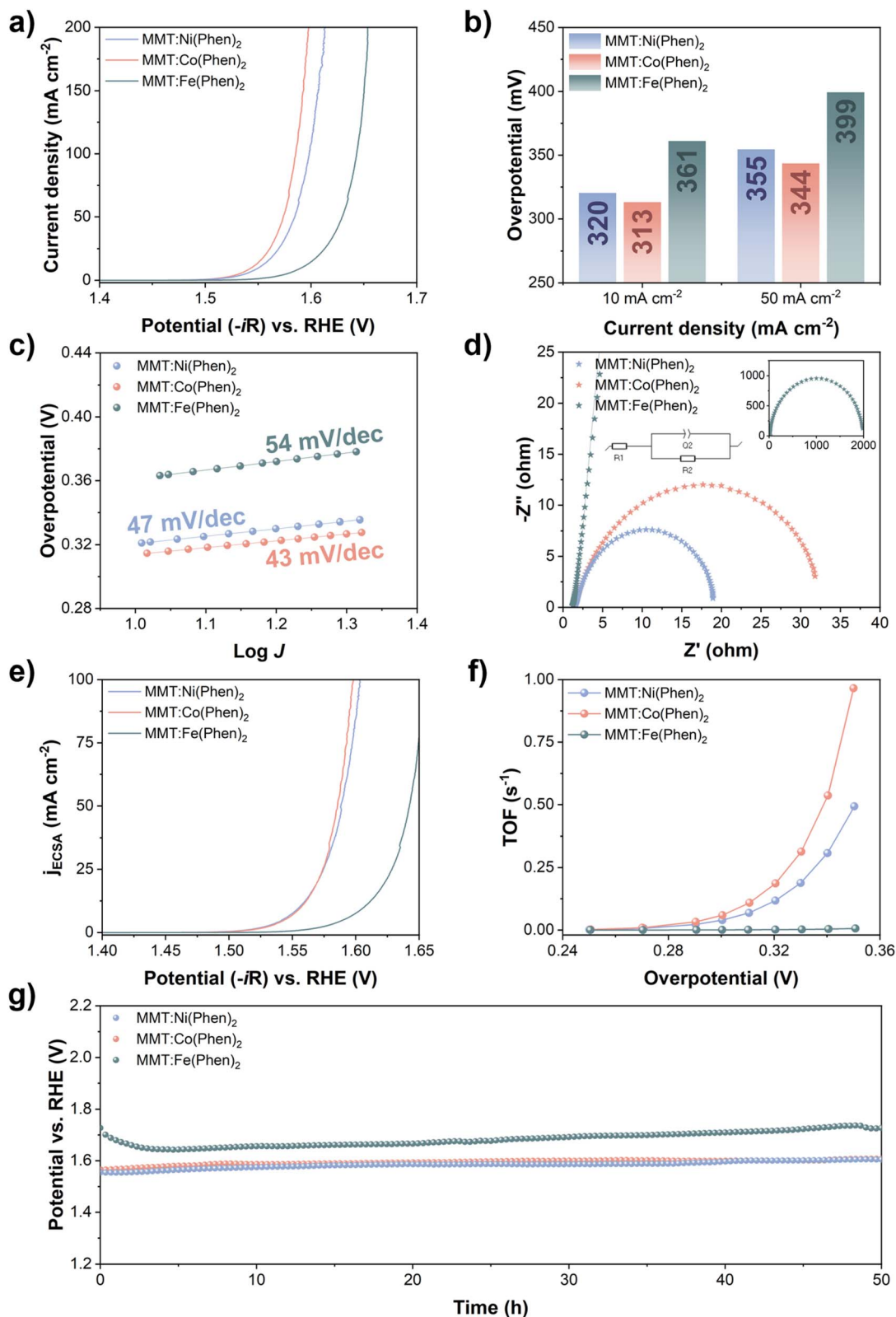


Fig. 4 Electrochemical OER performance of catalysts. (a) LSV curves, (b) overpotentials, (c) Tafel plots, (d) Nyquist plots (inset: equivalent circuit model), (e) ECSA-normalized LSV curves, (f) TOF curves, and (g) long-term stability tests of MMT:M(Phen)<sub>2</sub> at a current density of 10 mA cm<sup>-2</sup>.





activity may decrease. In contrast,  $\text{Co(Phen)}_2$  ( $d^7$ , low-spin) has a partially filled  $e_g$  orbital ( $t_{2g}^6 e_g^1$ ), which helps to moderate the strong interaction between the metal center and oxygen intermediates.<sup>39</sup> The presence of one  $e_g$  electron introduces slight electron repulsion, weakening the binding just enough to strike a better balance between oxygen intermediate stability.<sup>54</sup> This leads to improved charge transfer and faster reaction kinetics, as reflected in its lower Tafel slope and higher TOF.  $\text{Ni(Phen)}_2$  ( $d^8$ , low-spin) also follows a similar trend; however, due to the fully half-filled  $e_g$  orbitals ( $t_{2g}^6 e_g^2$ ), electron repulsion increases, leading to a weaker interaction with the oxygen intermediate.<sup>55</sup> This effect results in weaker oxygen adsorption compared to  $\text{Co(Phen)}_2$ , which may slightly reduce the OER efficiency relative to  $\text{Co(Phen)}_2$ .<sup>56</sup> Additionally, the electronic configuration of  $\text{Co}^{2+}$  and  $\text{Ni}^{2+}$  facilitates better charge transport compared to  $\text{Fe}^{2+}$ . The presence of an unpaired electron in  $\text{Co}^{2+}$  ( $d^7$ ,  $t_{2g}^6 e_g^1$ ) and  $\text{Ni}^{2+}$  ( $d^8$ ,  $t_{2g}^6 e_g^2$ ) enables electron hopping mechanisms, which can enhance electrical conductivity.<sup>1</sup> However, the lower-energy d-orbitals and greater availability of unoccupied states in  $\text{Co}^{2+}$  may contribute to faster charge transfer during the OER process, leading to better performance than  $\text{Ni(Phen)}_2$ .

Finally, chronopotentiometry (CP) measurements were performed to evaluate the long-term OER stability of the MMT:M(Phen)<sub>2</sub> catalysts (Fig. 4g). The results demonstrate that all three catalysts exhibit excellent stability, with negligible potential drift over the 50-hour test period. This stability highlights the robust structural and electrochemical properties of the MMT:M(Phen)<sub>2</sub> composites. In comparison, the stability tests for Na-MMT and MMT:Phen, shown in Fig. S7c,† reveal significantly higher potential drift, indicating reduced stability in the absence of transition metal incorporation. These findings underscore the role of the MMT framework and the coordinated transition metal in enhancing the long-term durability of the catalysts during OER operation, making them promising candidates for practical applications.

Compared with previously reported OER catalysts, the MMT:Co(Phen)<sub>2</sub> composite exhibits a competitive overpotential of 313 mV at 10 mA cm<sup>-2</sup>, outperforming many transition metal-based electrocatalysts (Fig. S9 and Table S7†). These findings establish MMT:Co(Phen)<sub>2</sub> as a promising catalyst with both high activity and long-term stability, making it a strong candidate for practical electrochemical applications.

### 3. Conclusions

This study successfully synthesized MMT-based electrocatalysts, MMT:M(Phen)<sub>2</sub>, and demonstrated their application in the OER. Transition metal–Phen organo-metallic complexes were effectively intercalated into the MMT interlayers using a simple sonication method, leveraging the high specific surface area and porous structure of MMT to enhance catalytic performance. The intercalation process increased the number of active sites and protected the organic ligands from degradation, thereby improving both the catalytic efficiency and the long-term stability of the materials. Among the synthesized catalysts, MMT:Co(Phen)<sub>2</sub> exhibited the best OER performance, achieving an overpotential of 313 mV at a current density of 10

mA cm<sup>-2</sup>. Furthermore, it demonstrated remarkable stability, maintaining a consistent potential over a 50-hour chronopotentiometry test at 10 mA cm<sup>-2</sup>. These results highlight the synergistic interaction between the transition metal and Phen ligand, as well as the structural advantages provided by the MMT matrix. Overall, this work provides a robust strategy for developing efficient and stable electrocatalysts through organo-metallic complex intercalation within layered clay materials. The MMT:M(Phen)<sub>2</sub> composites, particularly MMT:Co(Phen)<sub>2</sub>, show great potential for OER applications, paving the way for future advancements in energy conversion technologies.

## 4. Materials and methods

### 4.1 Materials

MMT K 10 was purchased from Sigma-Aldrich (USA), and 1,10-phenanthroline monohydrate was obtained from JUNSEI (Japan). Nickel nitrate hexahydrate ( $\text{Ni(NO}_3)_2 \cdot 6\text{H}_2\text{O}$ , 98.0%), cobalt nitrate hexahydrate ( $\text{Co(NO}_3)_2 \cdot 6\text{H}_2\text{O}$ , 97.0%), sodium chloride (NaCl, 99.5%), and hydrogen peroxide ( $\text{H}_2\text{O}_2$ , 34.5%) were sourced from Samchun (Korea). All chemicals used in this study were of analytical grade. All chemical reagents except for MMT K10 were used as received without further purification.

### 4.2 Purification of MMT

To remove carbonates from the MMT, the material was treated in a boiling water bath with a pH 5 sodium acetate/acetic acid buffer solution. Organic residues were subsequently eliminated using a hydrogen peroxide ( $\text{H}_2\text{O}_2$ ) solution. The MMT was then converted to Na-MMT by treating it with a 1 M NaCl solution, facilitating the insertion of  $\text{Na}^+$  ions between its layers. The Na-MMT was then thoroughly washed with distilled water to remove excess  $\text{Na}^+$  ions. Finally, the purified MMT was dried in an oven at 70 °C to complete the process.

### 4.3 Synthesis of MMT:Phen

The purified Na-MMT was modified *via* cation-exchanged with Phen in ethanol. For the synthesis, 0.5 g of Na-MMT and 1.5 g of Phen were dispersed in 50 mL ethanol using ultrasonication for one hour. The mixture was then placed in an oven at 70 °C for two weeks with daily ultrasonication for one hour to ensure proper dispersion during the reaction. After completion of the reaction, the product was washed multiple times *via* centrifugation with ethanol to remove excess Phen. Finally, MMT with Phen inserted between its layers (designated as MMT:Phen) was dried at 70 °C.

### 4.4 Synthesis of MMT:M(Phen)<sub>2</sub>

The synthesized MMT:Phen and the metal precursor ( $\text{Ni(NO}_3)_2 \cdot 6\text{H}_2\text{O}$ ,  $\text{Co(NO}_3)_2 \cdot 6\text{H}_2\text{O}$ , and  $\text{Fe(NO}_3)_3 \cdot 9\text{H}_2\text{O}$ ) were dispersed in 50 mL of ethanol at a mass ratio of 1 : 2. The mixture was sonicated for one hour and subsequently reacted in an oven at 70 °C for two weeks. During the reaction, the mixture was sonicated for one hour daily to maintain proper dispersion. Upon completion of the reaction, the product was thoroughly washed with ethanol to remove excess metal and nitrate ions.



Finally, the resulting MMT with metal-phenanthroline complexes inserted between its layers (designated MMT:M(Phen)<sub>2</sub> (M = Ni, Co, and Fe)) was dried at 70 °C.

#### 4.5 Characterization

Various electron microscopy and spectroscopy techniques were employed to analyze the surface structure of the synthesized catalysts. High resolution field emission scanning electron microscopy (HR FE-SEM; Carl Zeiss, LEOSUPRA 55), field emission transmission electron microscopy (FE-TEM; JEOL, JEM-2100F) and Cs-corrector transmission electron microscopy (Cs-TEM; JEOL, JEM-ARM200F) were utilized for the surface structure analyses. Energy-dispersive X-ray spectroscopy (EDS) measurements were conducted using the Oxford X-MAXN system attached to the FE-SEM equipment and the JEOL Dual SDD EDS system attached to the Cs-TEM. The crystalline structure was analyzed using an X-ray diffractometer (XRD; Bruker, D8 Advance) with Cu K $\alpha$  radiation at a scan rate of 3° min<sup>-1</sup>. Small-angle X-ray scattering (SAXS) measurements were performed using an X-ray diffractometer (SAXS; RIGAKU, NANOPIX) with Cu K $\alpha$  radiation. Surface chemical characterization was performed using X-ray photoelectron spectroscopy (XPS; Thermo Fisher Scientific, Thermo Electron) with monochromated Al K $\alpha$  radiation, and the spectra were adjusted for charging effects by setting the C-C bond of C 1s to a binding energy of 284.8 eV. Elemental analysis was conducted using inductively coupled plasma-mass spectrometry (ICP-MS; Agilent Technologies, 7800 ICP-MS). The molecular structure was analyzed using Fourier-transform infrared spectroscopy (FT-IR; PerkinElmer Spectrum One), with samples pretreated as salt pellets (with KBr) over a spectral range of 4000–400 cm<sup>-1</sup>. Thermogravimetric analysis (TGA) was performed using a thermogravimetric analyzer (Rigaku, STA8122) in an N<sub>2</sub> gas flow over the temperature range of 30–1000 °C. The specific surface area was measured using Brunauer-Emmett-Teller (BET) surface area analysis (BELSORP-max(MP)).

#### 4.6 Electrochemical measurements

Electrochemical activity was analyzed using a potentiostat (BioLogic, SP-300), configured in a three-electrode system, where the working electrode consisted of catalyst-coated PTFE-free carbon paper, Pt mesh served as the counter electrode, and Hg/HgO as the reference electrode.

For assessing the OER activity, the catalyst ink was prepared by dispersing 20 mg of the catalyst material, 5 mg of carbon black and 100  $\mu$ L of a 5 wt% Nafion solution in 5 mL ethanol. The dispersed ink was loaded onto a 5  $\times$  5 cm<sup>2</sup> carbon paper *via* spraying and then dried in a 70 °C oven. A 1 M KOH solution was used as electrolyte. The catalyst was activated by performing 50 repetitive measurements using CV from 0 to 1 V at a scan rate of 20 mV s<sup>-1</sup>, followed by measurements from 0 to 1 V at a scan rate of 10 mV s<sup>-1</sup>. EIS measurements were measured from 100 000 Hz to 0.001 Hz at a fixed potential of 0.59 V *versus* Hg/HgO reference electrode.

After electrochemical measurements, the potentials of the working electrodes were converted to reversible hydrogen electrode (RHE) scale for reporting.

$$E_{\text{RHE}} = E_{\text{Hg/HgO}} + 0.0592 \times \text{pH} + 0.098 - iR$$

The overpotential ( $\eta$ ) for the OER was calculated using the following equation:

$$\eta = E_{\text{RHE}} - 1.23$$

The Tafel slope was calculated based on using the equation:

$$\eta = a + b \log J,$$

where  $a$  is a constant,  $b$  is the Tafel slope,  $J$  is the current density.

The electric double layer capacitance ( $C_{\text{dl}}$ ) was measured using CV at various scan rates within the potential range of 0.92 to 1.02 V *versus* the RHE, and was determined using the equation:<sup>57</sup>

$$C_{\text{dl}} = \Delta j(j_a - j_c)/2\nu \quad (1)$$

where  $j_a$  and  $j_c$  are anodic and cathodic current densities at  $E = 0.97$  V and  $\nu$  is the scan rate in mV s<sup>-1</sup>. The ECSA was then calculated from the  $C_{\text{dl}}$  value, assuming the specific capacitance ( $C_s$ ) of  $\sim 40 \mu\text{F cm}^{-2}$  for a flat surface with 1.0 cm<sup>2</sup> of real surface area according to the following equation:<sup>58</sup>

$$\text{ECSA} = C_{\text{dl}}/C_s \quad (2)$$

TOF was calculated by assuming that all metal ions estimated from ICP-MS serve as active sites according to the following equation:<sup>59</sup>

$$\text{TOF} = j/(4 \times F \times n) \quad (3)$$

where  $j$ ,  $F$ , and  $n$  represent the current density, the Faraday constant (96 485 C mol<sup>-1</sup>), and the concentration of active sites (mol cm<sup>-2</sup>), respectively.

## Data availability

The data supporting this article have been included as part of the ESI.†

## Author contributions

In Seon Lee and Jae Ryeol Jeong contributed equally to this work. In Seon Lee: investigation, data curation, writing – original draft. Jae Ryeol Jeong: conceptualization, investigation, writing – original draft. Cu Dang Van: writing – review & editing. Min Hyung Lee: conceptualization, supervision, writing – review & editing, funding acquisition.





## Conflicts of interest

The authors declare no conflicts of interest.

## Acknowledgements

This work was financially supported by the “Carbon to X Project” (NRF-2020M3H7A1096388), and “The Basic Research Program” (NRF-2021R1A2C2010244) through the National Research Foundation of Korea (NRF) funded by the Ministry of Science and ICT.

## References

- 1 N. S. Lewis and D. G. Nocera, *Proc. Natl. Acad. Sci. U. S. A.*, 2006, **103**, 15729–15735.
- 2 Z. W. Seh, J. Kibsgaard, C. F. Dickens, I. Chorkendorff, J. K. Nørskov and T. F. Jaramillo, *Science*, 2017, **355**, eaad4998.
- 3 S. Chu and A. Majumdar, *Nature*, 2012, **488**, 294–303.
- 4 J. A. Turner, *Science*, 2004, **305**, 972–974.
- 5 B. You and Y. Sun, *Acc. Chem. Res.*, 2018, **51**, 1571–1580.
- 6 S. Perumal, I. Pokhrel, U. Muhammad, X. Shao, Y. Han, M. Kim and H. Lee, *ACS Mater. Lett.*, 2024, **6**, 3625–3666.
- 7 A. Hayat, M. Sohail, H. Ali, T. A. Taha, H. I. A. Qazi, N. Ur Rahman, Z. Ajmal, A. Kalam, A. G. Al-Sehemi, S. Wageh, M. A. Amin, A. Palamanit, W. I. Nawawi, E. F. Newair and Y. Orooji, *Chem. Rec.*, 2023, **23**, e202200149.
- 8 K. Oka, O. Tsujimura, T. Suga, H. Nishide and B. Winther-Jensen, *Energy Environ. Sci.*, 2018, **11**, 1335–1342.
- 9 X. Li, L. Zhao, J. Yu, X. Liu, X. Zhang, H. Liu and W. Zhou, *Nano-Micro Lett.*, 2020, **12**, 131.
- 10 W. Wang, M. Xu, X. Xu, W. Zhou and Z. Shao, *Angew. Chem., Int. Ed.*, 2020, **59**, 136–152.
- 11 X. Li, J. Yu, J. Jia, A. Wang, L. Zhao, T. Xiong, H. Liu and W. Zhou, *Nano Energy*, 2019, **62**, 127–135.
- 12 Y. Jiao, Y. Zheng, M. Jaroniec and S. Z. Qiao, *Chem. Soc. Rev.*, 2015, **44**, 2060–2086.
- 13 N.-T. Suen, S.-F. Hung, Q. Quan, N. Zhang, Y.-J. Xu and H. M. Chen, *Chem. Soc. Rev.*, 2017, **46**, 337–365.
- 14 Y. P. Zhu, C. Guo, Y. Zheng and S.-Z. Qiao, *Acc. Chem. Res.*, 2017, **50**, 915–923.
- 15 H. Jin, C. Guo, X. Liu, J. Liu, A. Vasileff, Y. Jiao, Y. Zheng and S.-Z. Qiao, *Chem. Rev.*, 2018, **118**, 6337–6408.
- 16 N. M. Marković, T. J. Schmidt, V. Stamenković and P. N. Ross, *Fuel Cells*, 2001, **1**, 105–116.
- 17 Y. Sasaki, H. Kato and A. Kudo, *J. Am. Chem. Soc.*, 2013, **135**, 5441–5449.
- 18 H. B. Gray, *Nat. Chem.*, 2009, **1**, 7.
- 19 K. Jlassi, I. Krupa and M. M. Chehimi, in *Clay-polymer Nanocomposites*, ed. K. Jlassi, M. M. Chehimi and S. Thomas, Elsevier, 2017, pp. 1–28.
- 20 C. V. Lazaratou, D. V. Vayenas and D. Papoulis, *Appl. Clay Sci.*, 2020, **185**, 105377.
- 21 V. B. Motalov, N. S. Karasev, N. L. Ovchinnikov and M. F. Butman, *J. Anal. Methods Chem.*, 2017, **2017**, 4984151.
- 22 K. Wen, J. Zhu, H. Chen, L. Ma, H. Liu, R. Zhu, Y. Xi and H. He, *Langmuir*, 2019, **35**, 382–390.
- 23 Y. Cardona, S. A. Korili and A. Gil, *Appl. Clay Sci.*, 2021, **203**, 105996.
- 24 G. B. B. Varadwaj and K. M. Parida, *RSC Adv.*, 2013, **3**, 13583–13593.
- 25 I. E. Odom, L. Fowden, R. M. Barrer and P. B. Tinker, *Philos. Trans. R. Soc., A*, 1984, **311**, 391–409.
- 26 G. M. Xu, M. Wang, H. L. Bao, P. F. Fang, Y. H. Zeng, L. Du and X. L. Wang, *Front. Chem.*, 2022, **10**, 916860.
- 27 G. Lv, Z. Li, W.-T. Jiang, P.-H. Chang and L. Liao, *Mater. Chem. Phys.*, 2015, **162**, 417–424.
- 28 Z. U. Zango, A. Garba, Z. N. Garba, M. U. Zango, F. Usman and J.-W. Lim, *Sustainability*, 2022, **14**, 16441.
- 29 E. Almadani, S. Radzi and F. Harun, *Int. J. Appl. Chem.*, 2016, **12**, 62–67.
- 30 S. Yang, Y. Ji, F. Deng, X. Sun and C. Ning, *J. Mater. Chem. B*, 2022, **10**, 3705–3715.
- 31 P. Cool and E. F. Vansant, in *Synthesis*, Springer Berlin Heidelberg, Berlin, Heidelberg, 1998, pp. 265–288.
- 32 A. Gil, M. A. Vicente and L. M. Gandía, *Microporous Mesoporous Mater.*, 2000, **34**, 115–125.
- 33 J. Zhu, K. Wen, Y. Wang, L. Ma, X. Su, R. Zhu, Y. Xi and H. He, *Microporous Mesoporous Mater.*, 2018, **265**, 104–111.
- 34 G. Tamiru, A. Abebe, M. Abebe and M. Liyew, *Ethiop. J. Sci. Technol.*, 2019, **12**, 69.
- 35 Q. Zeng, D. Z. Wang, A. Yu and M. Lu, *Nanotechnology*, 2002, **13**, 549–553.
- 36 R. Mokaya and W. Jones, *J. Catal.*, 1995, **153**, 76–85.
- 37 R. E. Swai, *J. Pet. Explor. Prod.*, 2020, **10**, 3515–3532.
- 38 P. T. Bertuoli, D. Piazza, L. C. Scienza and A. J. Zattera, *Appl. Clay Sci.*, 2014, **87**, 46–51.
- 39 J. Wang, Z. Zhao, M. Guo, L. Xiao, H. Tang, J. Li, Z. Kou and J. Li, *EES Catal.*, 2024, **2**, 862–873.
- 40 M. Gironès, L. A. M. Bolhuis-Versteeg, R. G. H. Lammertink and M. Wessling, *J. Colloid Interface Sci.*, 2006, **299**, 831–840.
- 41 P. Ying, G. Jin and Z. Tao, *Colloids Surf., B*, 2004, **33**, 259–263.
- 42 D. B. Jiang, C. Jing, Y. Yuan, L. Feng, X. Liu, F. Dong, B. Dong and Y. X. Zhang, *J. Colloid Interface Sci.*, 2019, **540**, 398–409.
- 43 J. Yao, R. Huang, J. Jiang, S. Xiao and Y. Li, *Ionics*, 2021, **27**, 1125–1135.
- 44 A. Jena, T. R. Penki, N. Munichandraiah and S. A. Shivashankar, *J. Electroanal. Chem.*, 2016, **761**, 21–27.
- 45 Y. Bai, W. Wang, R. Wang, J. Sun and L. Gao, *J. Mater. Chem. A*, 2015, **3**, 12530–12538.
- 46 D. Yao, Y. Shi, H. Pan, D. Zhong, H. Hou, X. Wu, J. Chen, L. Wang, Y. Hu and J. C. Crittenden, *Chem. Eng. J.*, 2020, **392**, 123637.
- 47 S. K. Bhorodwaj and D. K. Dutta, *Appl. Clay Sci.*, 2011, **53**, 347–352.
- 48 M. Shirzad-Siboni, A. Khataee, A. Hassani and S. Karaca, *C. R. Chim.*, 2015, **18**, 204–214.
- 49 G. Leofanti, M. Padovan, G. Tozzola and B. Venturelli, *Catal. Today*, 1998, **41**, 207–219.
- 50 I. A. Bakare, S. Adamu, M. Qamaruddin, S. A. Al-Bogami, S. Al-Ghamdi and M. M. Hossain, *Ind. Eng. Chem. Res.*, 2019, **58**, 10785–10792.



- 51 G. B. B. Varadwaj, S. Rana and K. M. Parida, *Dalton Trans.*, 2013, **42**, 5122–5129.
- 52 F. Harun, E. Almadani and S. Radzi, *Int. J. Sci. Res. Dev.*, 2016, **3**, 90–96.
- 53 Z. Chen, X. Li, H. Ma, Y. Zhang, J. Peng, T. Ma, Z. Cheng, J. Gracia, Y. Sun and Z. J. Xu, *Natl. Sci. Rev.*, 2024, **11**, nwae314.
- 54 J. Suntivich, K. J. May, H. A. Gasteiger, J. B. Goodenough and Y. Shao-Horn, *Science*, 2011, **334**, 1383–1385.
- 55 C. Hu, X. Wang, T. Yao, T. Gao, J. C. Han, X. Zhang, Y. Zhang and P. Xu, *Adv. Funct. Mater.*, 2019, **29**, 1902449.
- 56 Y. Yao, J. Lyu, X. Li, C. Chen, F. Verpoort, J. Wang, Z. Pan and Z. Kou, *DeCarbon*, 2024, **5**, 100062.
- 57 A. Karmakar and S. Kundu, *Mater. Today Energy*, 2023, **33**, 101259.
- 58 P. Connor, J. Schuch, B. Kaiser and W. Jaegermann, *Z. Phys. Chem.*, 2020, **234**, 979–994.
- 59 D. Tanwar, P. Jain, D. Ahluwalia, A. Sudheendranath, S. P. Thomas, P. P. Ingole and U. Kumar, *RSC Adv.*, 2023, **13**, 24450–24459.

